



1 **Long term variations of actual evapotranspiration over the Tibetan**

2 **Plateau**

3 Cunbo Han<sup>1,2</sup>, Yaoming Ma<sup>1,3,4,5</sup>, Binbin Wang<sup>1</sup>, Lei Zhong<sup>6</sup>, Weiqiang Ma<sup>1,3</sup>,

4 Xuelong Chen<sup>1,3</sup>, Zhongbo Su<sup>7</sup>

5 1. Key Laboratory of Tibetan Environment Changes and Land Surface

6 Processes, Institute of Tibetan Plateau Research, Chinese Academy of

7 Sciences, Chinese Academy of Sciences, Beijing, China

8 2. Institute for Meteorology and Climate Research, Karlsruhe Institute of

9 Technology, Karlsruhe, Germany

10 3. CAS Center for Excellence in Tibetan Plateau Earth Sciences, Chinese

11 Academy of Sciences, Beijing, China

12 4. University of Chinese Academy of Sciences, Beijing, China

13 5. Lanzhou University, Lanzhou, China

14 6. Laboratory for Atmospheric Observation and Climate Environment

15 Research, School of Earth and Space Sciences, University of Science

16 and Technology of China, Hefei, China

17 7. Faculty of Geo-Information Science and Earth Observation, University of

18 Twente, Enschede, The Netherlands

19

20 **Correspondence to:**

21 Prof. Dr. Yaoming Ma

22 Institute of Tibetan Plateau Research, Chinese Academy of Sciences

23 (ITPCAS)

24 16-3 Lincui Road, Chaoyang District, Beijing

25 100101, China

26

27 Tel: +86 010 84097079

28 Email: [yyma@itpcas.ac.cn](mailto:yyma@itpcas.ac.cn)



29 **Abstract**

30 Terrestrial actual evapotranspiration ( $ET_a$ ) is a key parameter controlling the  
31 land-atmosphere interaction processes and the water cycle. However, the  
32 spatial distribution and temporal changes of  $ET_a$  over the Tibetan Plateau (TP)  
33 remain very uncertain. Here we estimate the multiyear (2001-2018) monthly  
34  $ET_a$  and its spatial distribution on the TP by a combination of meteorological  
35 data and satellite products. Validation against data from six eddy-covariance  
36 monitoring sites yielded a root mean square errors ranging from 9.3 to 14.5  
37  $\text{mm mo}^{-1}$ , and correlation coefficients exceeding 0.9. The domain mean of  
38 annual  $ET_a$  on the TP decreased slightly ( $-1.45 \text{ mm yr}^{-1}$ ,  $p < 0.05$ ) from 2001  
39 to 2018. The annual  $ET_a$  increased significantly at a rate of  $2.62 \text{ mm yr}^{-1}$  ( $p <$   
40  $0.05$ ) in the eastern sector of the TP ( $\text{lon} > 90^\circ \text{ E}$ ), but decreased significantly  
41 at a rate of  $-5.52 \text{ mm yr}^{-1}$  ( $p < 0.05$ ) in the western sector of the TP ( $\text{lon} < 90^\circ$   
42  $\text{E}$ ). In addition, the decreases in annual  $ET_a$  were pronounced in spring and  
43 summer seasons, while almost no trends were detected in the autumn and  
44 winter seasons. The mean annual  $ET_a$  during 2001-2018 and over the whole  
45 TP was  $496 \pm 23 \text{ mm}$ . Thus, the total evapotranspiration from the terrestrial  
46 surface of the TP was  $1238.3 \pm 57.6 \text{ km}^3 \text{ yr}^{-1}$ . The estimated  $ET_a$  product  
47 presented in this study is useful for an improved understanding of changes in  
48 energy and water cycle on the TP. The dataset is freely available at the  
49 Science Data Bank (<http://www.dx.doi.org/10.11922/sciencedb.t00000.00010>,  
50 (Han et al. 2020)) and at the National Tibetan Plateau Data Center  
51 (<https://data.tpdc.ac.cn/en/data/5a0d2e28-ebc6-4ea4-8ce4-a7f2897c8ee6/>).

52

53 **Key words:** Actual evapotranspiration; SEBS; Tibetan Plateau; Trend.

54



55

56 **Key points:**

- 57       • The SEBS-estimated monthly  $ET_a$  during 2001-2018 shows acceptable  
58       accuracy validated against 6 flux towers.
- 59       • Annual  $ET_a$  over the entire TP and in the western TP decrease  
60       significantly, while it increases in the east TP.
- 61       • Decrease of annual  $ET_a$  is pronounced in spring and summer, while  
62       almost no trends are detected in autumn and winter.

63

64



## 65 1 Introduction

66 As the birthplace of Asia's major rivers, the Tibetan Plateau (TP), famous as  
67 the "Water Tower of Asia", is essential to the Asian energy and water cycles  
68 (Immerzeel et al. 2010, Yao et al. 2012). Along with increasing air  
69 temperature, evidence from the changes of precipitation, runoff, and soil  
70 moisture indicates that the hydrological cycle of the TP has been intensified  
71 during the past century (Yang et al. 2014). Contributing around two-thirds of  
72 global terrestrial precipitation, evapotranspiration (*ET*) is a crucial component  
73 that affects the exchange of water and energy between the land surface and  
74 the atmosphere (Oki and Kanae 2006, Fisher et al. 2017). *ET* is also an  
75 essential factor modulating regional and global weather and climate. As the  
76 only connecting component between the energy budget and the water cycle in  
77 the terrestrial ecosystems (Xu and Singh 2005), *ET* and variations of *ET* over  
78 the TP have received increasing attention worldwide (Xu and Singh 2005, Li  
79 et al. 2014, Zhang et al. 2018, Yao et al. 2019, Wang et al. 2020). Total  
80 evaporation from large lakes of the TP has been quantitatively estimated  
81 recently (Wang et al. 2020), however, the terrestrial *ET* on the TP and its  
82 spatial and temporal changes remain very uncertain.

83

84 Many studies have tried to evaluate *ET*'s temporal and spatial variability  
85 across the TP using various methods. The pan evaporation ( $E_{\text{pan}}$ ), that  
86 represents the amount of water evaporated from an open circular pan, is the  
87 most popular observational data source of *ET*. Long time series of  $E_{\text{pan}}$  are  
88 often available with good comparability among various regional  
89 measurements. Thus, it has been widely used in various disciplines, e.g.,  
90 meteorology, hydrology, and ecology. Several studies have revealed the trend  
91 of  $E_{\text{pan}}$  on the TP (Zhang et al. 2007, Liu et al. 2011, Shi et al. 2017, Zhang et  
92 al. 2018, Yao et al. 2019). Although  $E_{\text{pan}}$  and potential *ET* suggest the long-



93 term variability of  $ET$  according to contrasting trends between  $E_{pan}$  and actual  
94  $ET$  ( $ET_a$ ) (Zhang et al. 2007), these measures cannot precisely depict the  
95 spatial pattern of trends in  $ET_a$ . Recently, several studies applied revised  
96 models, which are based on the complementary relationship (CR) of  $ET$ , to  
97 estimate  $ET_a$  on the TP (Zhang et al. 2018, Ma et al. 2019, Wang et al. 2020).  
98 Employing only routine meteorological observations without requiring any  
99 vegetation and soil information is the most significant advantage of CR  
100 models (Szilagyi et al. 2017). However, numerous assumptions and  
101 requirements of validations of key parameters limit the application and  
102 performance of CR models over different climate conditions. The application  
103 of eddy-covariance (EC) technologies in the past decade has dramatically  
104 advanced our understanding of the terrestrial energy balance and  $ET_a$  over  
105 various ecosystems across the TP. However, the fetch of the EC observation  
106 is on the order of hundreds of meters, thus impeding the ability to capture the  
107 plateau-scale variations of  $ET_a$ . Therefore, finding an effective way to advance  
108 the estimation of  $ET_a$  on the TP is of great importance.

109

110 Satellite remote sensing (RS) provides temporally frequent and spatially  
111 contiguous measurements of land surface characteristics that affect  $ET$ , for  
112 example, land surface temperature, albedo, vegetation index. Satellite RS  
113 also offers the opportunity to retrieve  $ET$  over a heterogeneous surface  
114 (Zhang et al. 2010). Multiple RS-based algorithms have been proposed.  
115 Among these algorithms, the surface energy balance system (SEBS)  
116 proposed by Su (2002) has been widely applied to retrieve land surface  
117 turbulent fluxes on the TP (Chen et al. 2013, Ma et al. 2014, Han et al. 2016,  
118 Han et al. 2017, Zou et al. 2018, Zhong et al. 2019). Chen et al. (2013)  
119 improved the roughness length parameterization scheme for heat transfer in  
120 SEBS to expand its modeling applicability over bare ground, sparse canopy,



121 dense canopy, and snow surfaces in the TP. An algorithm for effective  
122 aerodynamic roughness length had been introduced into the SEBS model to  
123 parameterize subgrid-scale topographical form drag (Han et al. 2015, Han et  
124 al. 2017). This scheme improved the skill of the SEBS model in estimating the  
125 surface energy budget over mountainous regions of the TP. A recent advance  
126 by Chen et al. (2019) optimized five critical parameters in SEBS using  
127 observations collected from 27 sites globally, including 6 sites on the TP, and  
128 suggested that the overestimation of the global  $ET$  was substantially improved  
129 with the use of optimal parameters.

130

131 While the spatial and temporal pattern of the  $ET_a$  in the TP had been  
132 investigated in many studies (Zhang et al. 2007, Zhang et al. 2018, Wang et  
133 al. 2020), considerable inconsistencies for both trends and magnitudes of  $ET_a$   
134 exist due to uncertainties in forcing and parameters used by various models.  
135 Thus, in this study, with full consideration of the recent developments in the  
136 SEBS model over the TP, we aim to (1) develop an 18-year (2001-2018)  $ET_a$   
137 product of the TP, along with independent validations against EC  
138 observations; (2) quantify the spatiotemporal variability of the  $ET_a$  in the TP,  
139 and (3) uncover the main factors dominating the changes in  $ET_a$ , using the  
140 estimated product.

141

## 142 **2 Methodology and data**

### 143 **2.1 Model description**

144 The SEBS model (Su 2002) was used to derive land surface energy flux  
145 components in the present study. The remote-sensed land surface energy  
146 balance equation is given by



147 
$$R_n = H + LE + G_0. \quad (1)$$

148  $R_n$  is the net radiation flux ( $\text{W m}^{-2}$ ),  $H$  is the sensible heat flux ( $\text{W m}^{-2}$ ),  $LE$  is  
149 the latent heat flux ( $\text{W m}^{-2}$ ), and  $G_0$  is the ground heat flux ( $\text{W m}^{-2}$ ).

150

151 The land surface net radiation flux was computed as

152 
$$R_n = (1 - \alpha) \times SWD + LWD - \varepsilon \times \sigma \times T_s^4 \quad (2)$$

153 where  $\alpha$  is the land surface albedo derived from the Moderate Resolution  
154 Imaging Spectroradiometer (MODIS) products. Downward shortwave ( $SWD$ )  
155 and longwave ( $LWD$ ) radiation were obtained from the China Meteorological  
156 Forcing Dataset (CMFD). Land surface temperature ( $T_s$ ) and emissivity ( $\varepsilon$ )  
157 values were also obtained from MODIS products.

158

159 In vegetated areas the soil heat flux,  $G_0$ , was calculated from the net radiation  
160 flux and vegetation cover

161 
$$G_0 = R_n \times (r_c \times f_c + r_s \times (1 - f_c)). \quad (3)$$

162  $r_s$  and  $r_c$  are ratios of ground heat flux and net radiation for surfaces with bare  
163 soil and full vegetation, respectively. Fractional vegetation cover ( $f_c$ ) was  
164 derived from the normalized difference vegetation index (NDVI). Over water  
165 surfaces ( $\text{NDVI} < 0$  and  $\alpha < 0.47$ ),  $G_0 = 0.5R_n$  was used (Gao et al. 2011,  
166 Chen et al. 2013). On glaciers,  $G_0$  is negligible (Yang et al. 2011) and  $G_0 =$   
167  $0.05R_n$ .

168

169 In the atmospheric surface layer, sensible heat flux and friction velocity were  
170 calculated based on the Monin-Obukhov similarity (Stull 1988),

171 
$$U = \frac{u_*}{\kappa} \left[ \ln \left( \frac{z-d_0}{z_{0m}^{eff}} \right) - \psi_m \left( \frac{z-d_0}{L} \right) + \psi_m \left( \frac{z_{0m}^{eff}}{L} \right) \right] \quad (4)$$

172 
$$\theta_0 - \theta_a = \frac{H}{\kappa u_* \rho c_p} \left[ \ln \left( \frac{z-d_0}{z_{0h}^{eff}} \right) - \psi_h \left( \frac{z-d_0}{L} \right) + \psi_h \left( \frac{z_{0h}^{eff}}{L} \right) \right] \quad (5)$$

173 
$$L = \frac{\rho c_p u_*^3 \theta_v}{\kappa g H}. \quad (6)$$



174  $U$  is the horizontal wind velocity at a reference height  $z$  (m) above the ground  
175 surface,  $\theta_0$  is the potential temperature at the land surface (K),  $\theta_a$  is the  
176 potential temperature (K) at the reference height  $z$ ,  $d_0$  is the zero-plane  
177 displacement height (m),  $\rho$  is the air density ( $\text{kg m}^{-3}$ ),  $C_p$  is the specific heat for  
178 moist air ( $\text{J kg}^{-1} \text{ }^\circ\text{C}^{-1}$ ),  $\kappa = 0.4$  is the von Kármán's constant,  $u^*$  is the friction  
179 velocity,  $L$  is the Monin-Obukhov length (m),  $\theta_v$  is the potential virtual  
180 temperature (K) at the reference height  $z$ ,  $\psi_m$  and  $\psi_h$  are the stability  
181 correction functions for momentum and sensible heat transfer respectively,  
182 and  $g$  is the gravity acceleration ( $\text{m s}^{-2}$ ). To account for the form drag caused  
183 by subgrid-scale topographical obstacles, effective roughness lengths for  
184 momentum ( $z_{0m}^{\text{eff}}$ , m) and sensible heat ( $z_{0h}^{\text{eff}}$ , m) transfer were introduced into  
185 the SEBS model by Han et al. (2017). These modifications are parameterized  
186 as follows (Grant and Mason 1990, Han et al. 2015),

$$187 \quad \ln^2(h/2z_{0m}^{\text{eff}}) = \frac{\kappa^2}{0.5D\lambda + \kappa^2 / \ln^2(h/2z_{0m})} \quad (7)$$

$$188 \quad \ln(h/2z_{0h}^{\text{eff}} + 1) = \ln(h/2z_{0h} + 1) \frac{\ln(h/2z_{0m} + 1)}{\ln(h/z_{0m}^{\text{eff}} + 1)} \quad (8)$$

189 where  $\lambda$  is the average density of the subgrid-scale roughness elements  
190 calculated from digital elevation models,  $D$  is the form drag coefficient and  
191  $D=0.4$  is used for the mountainous areas of the TP as suggested by Han et al.  
192 (2015),  $z_{0m}$  and  $z_{0h}$  are the local-scale roughness lengths for momentum (m)  
193 and heat transfer (m), respectively. Detailed calculations can be found in Su  
194 (2002). A revised algorithm for  $z_{0h}$  developed by Chen et al. (2013) was  
195 applied as this algorithm outperforms the original scheme of the SEBS model  
196 on the TP.

197  
198 To constrain the actual evapotranspiration, an evaporative fraction was  
199 applied in the SEBS model. Under the dry-limit condition, the evaporation  
200 becomes zero due to the limited supply of available soil moisture, while water  
201 vapor evaporates at the potential rate under the wet-limit condition (Su 2002).



202 Finally, daily  $ET_a$  was calculated using the evaporative fraction as a residual of  
203 the surface energy budget equation while accounting for dry and wet limits.  
204 Details are available in Su (2002).

## 205 **2.2 Data**

206 In-situ observations, satellite-based products, and meteorological forcing data  
207 were used in this study to estimate monthly  $ET_a$  over the TP area. The CMFD,  
208 that was developed based on the released China Meteorological  
209 Administration (CMA) data (He et al. 2020), was used as model input. The  
210 CMFD covers the whole landmass of China at a spatial resolution of  $0.1^\circ$  and  
211 a temporal resolution of three hours. The dataset was established through the  
212 fusion of in-situ observations, remote sensing products, and reanalysis  
213 datasets. In particular, the dataset benefits from the merging of the  
214 observations at about 700 CMA's weather stations, and by using the Global  
215 Energy and Water Cycle Experiment – Surface Radiation Budget (GEWEX-  
216 SRB) shortwave radiation dataset (Pinker and Laszlo 1992). The GEWEX-  
217 SRB data has not been used in any other reanalysis dataset. In addition,  
218 independent datasets observed in western China where weather stations are  
219 scarce were used to evaluate the CMFD. This includes data collected through  
220 the Heihe Watershed Allied Telemetry Experimental Research (HiWATER) (Li  
221 et al. 2013) and the Coordinated Enhanced Observing Period (CEOP) Asia-  
222 Australia Monsoon Project (CAMP) (Ma et al. 2003). CMFD dataset is suitable  
223 for our study due to its continuous-time coverage and consistent quality.  
224 Detailed information for the CMFD dataset is listed in Table 1.

225

226 In-situ EC data observed at six flux stations on the TP were used to validate  
227 model results. Locations of the six observation sites are illustrated in Figure 1  
228 and detailed descriptions for these six sites are shown in Table 2. The



229 instrumental setup at each site consists of: an EC system comprising a sonic  
230 anemometer (CSAT3, Campbell Scientific Inc) and an open-path gas analyzer  
231 (LI-7500, Li-COR); a four-component radiation flux system (CNR-1, Kipp &  
232 Zonen), installed at a height of 1.5 m; a soil heat flux plate (Hukseflux,  
233 HFP01), buried in the soil to a depth of 0.1 m; soil moisture and temperature  
234 probes, buried at a depth of 0.05, 0.10, and 0.15 m, respectively (Han et al.  
235 2017). The EC data were processed with the EC software package TK3  
236 (Mauder and Foken 2015). The main post-processing procedures were as  
237 follows: spike detection, coordinate rotation, spectral loss correction,  
238 frequency response corrections (Moore 1986), and corrections for density  
239 fluctuations (Webb et al. 1980). The ground heat flux was obtained by  
240 summing the flux value observed by the heat flux plate and the energy  
241 storage in the layer above the heat flux plate (Han et al. 2016). Monthly EC  
242 data, which are used for validation, were generated from half-hourly variables.  
243 A more comprehensive dataset including the EC data used in this work has  
244 been published and is freely available (Ma et al. 2020).

### 245 **2.3 Model evaluation metrics and data analysis methods**

246 The model performance was assessed using the Pearson correlation  
247 coefficient ( $R$ ), the root mean square error (RMSE), and the mean bias (MB)  
248 between the estimated and observed monthly  $ET_a$  at the six stations on the  
249 TP.

250

251 The least-square regression technique was used to detect the long-term linear  
252 annual trends in  $ET_a$  values. The linear model to simulate  $ET_a$  values ( $Y_t$ )  
253 against time ( $t$ ) is

$$254 \quad Y_t = Y_0 + bt + \varepsilon_t \quad (9)$$

255



256 The Student's *t*-test, having an  $n-2$  degree of freedom ( $n$  is the number of  
257 samples), was used to evaluate the statistical significance of the linear  
258 trends, and only tests with a  $p$ -value less than 0.05 were selected as having  
259 passed the significance test.

### 260 **3 Results and discussion**

#### 261 **3.1 Validation against flux tower observations**

262 The SEBS-estimated  $ET_a$  was validated against EC observations at the six  
263 flux stations on the TP at a monthly scale (Figure 2). The SEBS model is  
264 capable of capturing both the magnitude and phase of the monthly  $ET_a$  signal  
265 at all the six stations. The correlation coefficients are all larger than 0.9 and  
266 have passed the significance test at the  $p = 0.01$  level. RMSE values range  
267 from 9.3 to 14.5 mm mo<sup>-1</sup> with the minimum at the BJ station and the  
268 maximum at the SETORS station. The MB values are all negative except at  
269 the NADORS station, which means the SEBS model slightly underestimated  
270  $ET_a$  values on the TP.

271

272 Specifically, the SEBS model performed particularly well at the sparse grass  
273 stations (NADORS and MAWORS) and at the short grass sites (BJ and  
274 NAMORS). At the high grass site (SETORS) and the gravel site (QOMS), the  
275 SEBS model is capable of reproducing the EC-observed monthly  $ET_a$  with  
276 RMSE values of 14.5 and 13.2 mm mo<sup>-1</sup>, respectively. In addition, the  
277 underestimates of  $ET_a$  by SEBS are mostly in the dry season, when the  
278 canopy is withered. The validation at the site-scale indicates that the SEBS  
279 model used in this work can be applied to a wide range of ecosystems over  
280 the TP.



### 281 3.2 Spatial distribution

282 There was a clear spatial pattern to the multiyear (2001-2018) mean annual  
283  $ET_a$  (Figure 3). In general, the SEBS-estimated  $ET_a$  decreases from the  
284 southeast to the northwest of the TP, with the maximum value above 1200  
285 mm in the southeastern Tibet and Hengduan Mountains and the minimum  
286 value less than 100 mm in the northwestern edge of the TP. In the central TP,  
287 where there are several lakes,  $ET_a$  was typically from 500 to 1000 mm.  $ET_a$   
288 was lower than 200 mm over the high, snow- and ice-bound, mountainous  
289 areas. For example, over the northern slopes of the Himalaya, Nyenchen  
290 Tanglha Mountains, and the eastern section of the Tanggula Mountains. The  
291 reason is that these snow- and ice-bound mountainous areas have a higher  
292 ability to reflect downward shortwave radiation and hence have less available  
293 energy to evaporate. On the whole, the domain averaged multiyear mean  
294 annual  $ET_a$  over the TP is  $496 \pm 23$  mm. The total amount of water  
295 evapotranspired from the terrestrial surface of the TP are around  
296  $1238.3 \pm 57.6 \text{ km}^3 \text{ yr}^{-1}$ , considering the area of the TP to be  $2.5 \times 10^6 \text{ km}^2$ .

297  
298 Figure 4 shows the multi-year average spring (March, April, and May), summer  
299 (June, July, and August), autumn (September, October, and November), and  
300 winter (December, January, and February)  $ET_a$  on the TP. Generally, the  
301 distribution pattern of seasonal  $ET_a$  was comparable with that of the annual  
302  $ET_a$ . Both seasonal and annual  $ET_a$  show a decreasing trend from the  
303 southeastern TP to the northwestern TP. Note that the distribution pattern  
304 almost faded out in winter season owing to a minimum in available energy  
305 and precipitation (Figure 4d). The  $ET_a$  in spring is higher than that in autumn,  
306 except for some high mountainous areas (e.g.: mountain ranges of Himalaya  
307 and Hengduan mountains). The spring  $ET_a$  ranges from 50 mm to 450 mm,  
308 while autumn  $ET_a$  ranges from 50 mm to 250 mm. In summer, the  $ET_a$  is



309 larger than 250 mm in most of the TP, while the  $ET_a$  is still below 100 mm in  
310 large areas of the northwestern TP. The multiyear seasonal  $ET_a$  averaged  
311 over the whole TP is  $140\pm 10$  mm,  $256\pm 12$  mm,  $84\pm 5$  mm, and  $34\pm 4$  mm, for  
312 spring, summer, autumn, and winter, respectively.

### 313 3.3 Trend analysis

314 The trend of annual  $ET_a$  during 2001-2018 is shown in Figure 5. Overall, an  
315 increasing trend of SEBS-simulated  $ET_a$  is dominant in the eastern TP (lon >  
316  $90^\circ$  E) while a decreasing trend is dominant in the western TP (lon <  $90^\circ$  E).  
317 The trends pass the  $t$ -test ( $p < 0.05$ ) in most part of the areas. The decreasing  
318 trend in the western TP is pronounced and passes the  $t$ -test ( $p < 0.05$ ). This  
319 trend is larger than  $-7.5$  mm  $yr^{-1}$  in most parts of the area and even larger than  
320  $-10$  mm  $yr^{-1}$  in a few parts. In the eastern TP, the increasing trend is mostly  
321 between 5 and 10 mm  $yr^{-1}$  and passes the  $t$ -test ( $p < 0.05$ ). The  $ET_a$  trend  
322 tends to be greater along the marginal region of the northern, eastern, and  
323 southeastern TP. Along the marginal region of the southwestern TP and in the  
324 western section of Himalaya Mountains this trend weakens.

325  
326 The trends of seasonal  $ET_a$  between 2001 and 2018 are spatially  
327 heterogeneous over the TP (Figure 6). Decreasing trends in spring and  
328 summer are generally at a rate between  $-2.5$  and  $-7.5$  mm  $yr^{-1}$ , and increasing  
329 trends are generally at a rate below 5.0 mm  $yr^{-1}$  and 7.5 mm  $yr^{-1}$  in spring and  
330 summer, respectively. Areas showing decreasing  $ET_a$  tend to become larger in  
331 autumn and winter seasons. Both the decreasing and increasing trends are  
332 subdued in autumn and winter compared with that in spring and summer  
333 seasons. Decreasing rates of  $ET_a$  in autumn and winter are generally below -  
334 2.5 mm  $yr^{-1}$ , and only a few areas have a rate larger than  $-2.5$  mm  $yr^{-1}$ .  
335



336 Due to the contrast in the trends in the eastern and western halves of the TP,  
337 we divided the TP into two regions: the eastern TP ( $\text{lon} > 90^\circ \text{E}$ ) and the  
338 western TP ( $\text{lon} < 90^\circ \text{E}$ ). Trends of the  $ET_a$  anomaly averaged over the entire  
339 TP, the western TP, and the eastern TP are shown in Figure 7a. The domain  
340 means of  $ET_a$  on the TP as a whole, and in the western TP decreased at rates  
341 of  $-1.45 \text{ mm yr}^{-1}$  and  $-5.52 \text{ mm yr}^{-1}$ , respectively. However, the  $ET_a$  in the  
342 eastern TP increased at a rate of  $2.62 \text{ mm yr}^{-1}$ . The decreasing rate of  $ET_a$  in  
343 the entire TP is influenced mainly by the significant decrease of  $ET_a$  in the  
344 western TP. Seasonally, the rates of change of  $ET_a$  over the whole TP are -  
345  $0.82 \text{ mm yr}^{-1}$  ( $p < 0.05$ ) and  $-0.79 \text{ mm yr}^{-1}$  ( $p < 0.05$ ) in spring and summer,  
346 respectively (Figure 7b). However, in autumn and winter the  $ET_a$  changes at a  
347 rate of  $0.10 \text{ mm yr}^{-1}$  and  $0.06 \text{ mm yr}^{-1}$ , respectively, and do not pass the  $t$ -test  
348 ( $p < 0.05$ ).  $ET_a$  in spring and summer seasons account for 75.7% of the  
349 annual  $ET_a$ . The variation in amplitude and changing rates in these two  
350 seasons are much larger than in the other seasons. Moreover, spatial  
351 distributions of spring and summer  $ET_a$  trends are close to that of the annual  
352  $ET_a$  trend (Figure 6). Thus, changes of  $ET_a$  in the spring and summer  
353 dominate the variations of  $ET_a$  in the whole year.

354

355 The decrease of  $ET_a$  over the whole TP and in the western TP during 2001-  
356 2018 can be explained by the decrease of  $R_n$  in the same time period (Figure  
357 8a). From 2001 to 2012,  $ET_a$  averaged over the entire TP increased slightly  
358 and then decreased dramatically from 2012, reaching a minimum in 2014.  
359 The significant decrease in  $ET_a$  between 2012 and 2014 was due to the rapid  
360 decline of the  $R_n$  (Figure 8a). In the eastern TP,  $ET_a$  increased during 2001-  
361 2018, while  $R_n$  decreased in the same period. Thus,  $R_n$  was not the dominant  
362 factor controlling the annual variations of  $ET_a$ . However, the increasing trends  
363 of both precipitation and air temperature can explain the increase of  $ET_a$  in the



364 eastern TP during the period 2001-2018 (Figure 8b and Figure 8c). The  
365 increasing precipitation increased the water resource available for  $ET_a$ .  
366 Moreover, the increasing air temperature accelerated the melting of  
367 permafrost and glaciers on the TP. Hence, the melting water replenished the  
368 ecosystem and increased the  $ET_a$  of the eastern TP.

369  
370 Although the domain-averaged trend in  $ET_a$  has been decreasing across the  
371 entire TP from 2001 to 2018,  $ET_a$  values in some areas have increased.  
372 Moreover, the changing rates also depend on the time series of  $ET_a$ . For  
373 example, the  $ET_a$  increased slightly from 2001 to 2012, while decreased from  
374 2001 to 2018. This demonstrates the necessity to utilize high-spatial  
375 resolution datasets and long time series to investigate the trends in  $ET_a$  over  
376 the TP.

#### 377 **4 Summary and conclusions**

378 The SEBS-estimated  $ET_a$  is at a resolution of around 10 km, while the  
379 footprint of EC observed  $ET_a$  values ranges from a few dozen meters to a few  
380 hundreds of meters. SEBS-estimated  $ET_a$  compares very well with  
381 observations at the six flux towers, showing low RMSE and MB values. These  
382 estimates were able to capture annual and seasonal variations in  $ET_a$ , despite  
383 these two datasets being mismatched in their spatial representation.

384  
385 Heterogeneous land surface characteristics and nonlinear changes in  
386 atmospheric conditions resulted in heterogeneities in spatial distributions of  
387  $ET_a$  and changes in  $ET_a$ . The SEBS-estimated multiyear (2001-2018) mean  
388 annual  $ET_a$  on the TP was  $515 \pm 22$  mm, resulting in approximately  
389  $1287.5 \pm 55.0$  km<sup>3</sup> yr<sup>-1</sup> of total water evapotranspiration from the terrestrial  
390 surface. Annual  $ET_a$  generally decreased from the southeast to the northwest



391 of the TP. The maximum was over 1200 mm, in the southeastern Tibet and  
392 Hengduan Mountains, while the minimum was less than 100 mm in the  
393 northwest marginal area of the TP. Moreover,  $ET_a$  was typically lower than 200  
394 mm over snow- and ice-bound mountainous areas, as there was limited  
395 available energy to evaporate the water.

396  
397 Averaged over the entire TP, annual  $ET_a$  increased slightly from 2001 to 2012,  
398 but decreased significantly after 2012 and reached a minimum in 2014.  
399 Generally, there was a slight decreasing trend in the domain mean annual  $ET_a$   
400 on the TP at the rate of  $-1.45 \text{ mm yr}^{-1}$  ( $p < 0.05$ ) from 2001 to 2018. However,  
401 trends of annual  $ET_a$  were opposite in the western and eastern TP. The  
402 annual  $ET_a$  decreased significantly in the western TP at a rate of  $-5.52 \text{ mm yr}^{-1}$   
403 ( $p < 0.05$ ) from 2001 to 2018, while annual  $ET_a$  in the eastern TP increased  
404 at a rate of  $2.62 \text{ mm yr}^{-1}$  ( $p < 0.05$ ) in the same period.

405  
406 The spatial distributions of seasonal  $ET_a$  trends were also noticeably  
407 heterogeneous during 2001-2018. The spatial patterns of rate of change of  
408  $ET_a$  in spring and summer were similar to the annual changes in  $ET_a$ . Finally,  
409  $ET_a$  decreased as well in the spring and summer season but at slower rates  
410 compared with the annual  $ET_a$ , however, only very weak trends were found in  
411 the autumn and winter seasons.

412

## 413 **5 Data availability**

414 The dataset presented and analyzed in this article has been released and is  
415 available for free download from the Science Data Bank  
416 (<http://www.dx.doi.org/10.11922/sciencedb.t00000.00010>, (Han et al. 2020))  
417 and from the National Tibetan Plateau Data Center



418 (<https://data.tpdc.ac.cn/en/data/5a0d2e28-ebc6-4ea4-8ce4-a7f2897c8ee6/>).

419 The dataset is published under the Creative Commons Attribution 4.0

420 International (CC BY 4.0) license.

421

#### 422 **Acknowledgments**

423 This study was funded by the Second Tibetan Plateau Scientific Expedition  
424 and Research (STEP) program (grant no. 2019QZKK0103), the Strategic  
425 Priority Research Program of Chinese Academy of Sciences (XDA20060101),  
426 the National Natural Science Foundation of China (91837208, 41705005, and  
427 41830650). The CMFD data were obtained from the National Tibetan Plateau  
428 Data Center (<https://data.tpdc.ac.cn/en/data/8028b944-daaa-4511-8769-965612652c49/>). MODIS data were obtained from the NASA Land Processes  
429 Distributed Active Archive Center (<https://lpdaac.usgs.gov/>). Global 1 km  
430 forest canopy height data were obtained from the Oak Ridge National  
431 Laboratory Distributed Active Archive Center for Biogeochemical Dynamics  
432 ([https://daac.ornl.gov/cgi-bin/dsvviewer.pl?ds\\_id=1271](https://daac.ornl.gov/cgi-bin/dsvviewer.pl?ds_id=1271)). The authors would like  
433 to thank all colleagues working at the observational stations on the TP for their  
434 maintenance of the instruments.

435

436

437



438        **References**

- 439        Chen, X., Z. Su, Y. Ma and E. M. Middleton. 2019. Optimization of a remote sensing energy balance  
440                method over different canopy applied at global scale. *Agricultural and Forest Meteorology* 279:  
441                107633-107633.
- 442        Chen, X., Z. Su, Y. Ma, K. Yang and B. Wang. 2013. Estimation of surface energy fluxes under complex  
443                terrain of Mt. Qomolangma over the Tibetan Plateau. *Hydrol. Earth Syst. Sci.* 17(4): 1607-1618.
- 444        Chen, X., Z. Su, Y. Ma, K. Yang, J. Wen and Y. Zhang. 2013. An Improvement of Roughness Height  
445                Parameterization of the Surface Energy Balance System (SEBS) over the Tibetan Plateau. *Journal*  
446                *of Applied Meteorology and Climatology* 52(3): 607-622.
- 447        Fisher, J. B., F. Melton, E. Middleton, C. Hain, M. Anderson, R. Allen, M. F. McCabe, S. Hook, D.  
448                Baldocchi, P. A. Townsend, A. Kilic, K. Tu, D. D. Miralles, J. Perret, J.-P. Lagouarde, D. Waliser, A.  
449                J. Purdy, A. French, D. Schimel, J. S. Famiglietti, G. Stephens and E. F. Wood. 2017. The future of  
450                evapotranspiration: Global requirements for ecosystem functioning, carbon and climate feedbacks,  
451                agricultural management, and water resources. *Water Resources Research* 53(4): 2618-2626.
- 452        Gao, Z. Q., C. S. Liu, W. Gao and N. B. Chang. 2011. A coupled remote sensing and the Surface Energy  
453                Balance with Topography Algorithm (SEBTA) to estimate actual evapotranspiration over  
454                heterogeneous terrain. *Hydrol. Earth Syst. Sci.* 15(1): 119-139.
- 455        Grant, A. L. M. and P. J. Mason. 1990. Observations of boundary-layer structure over complex terrain.  
456                *Quarterly Journal of the Royal Meteorological Society* 116(491): 159-186.
- 457        Han, C., Y. Ma, X. Chen and Z. Su. 2016. Estimates of land surface heat fluxes of the Mt. Everest region  
458                over the Tibetan Plateau utilizing ASTER data. *Atmospheric Research* 168: 180-190.
- 459        Han, C., Y. Ma, X. Chen and Z. Su. 2017. Trends of land surface heat fluxes on the Tibetan Plateau from  
460                2001 to 2012. *International Journal of Climatology* 37(14): 4757-4767.
- 461        Han, C., Y. Ma, Z. Su, X. Chen, L. Zhang, M. Li and F. Sun. 2015. Estimates of effective aerodynamic  
462                roughness length over mountainous areas of the Tibetan Plateau. *Quarterly Journal of the Royal*  
463                *Meteorological Society* 141(689): 1457-1465.
- 464        Han, C., Y. Ma, B. Wang, L. Zhong, W. Ma, X. Chen and Z. Su. 2020. The estimated actual  
465                evapotranspiration over the Tibetan Plateau from 2001 to 2018. *V1. Science Data Bank.*  
466                <http://www.dx.doi.org/10.11922/sciencedb.t00000.00010>.
- 467        He, J., K. Yang, W. Tang, H. Lu, J. Qin, Y. Chen and X. Li. 2020. The first high-resolution meteorological  
468                forcing dataset for land process studies over China. *Scientific Data* 7(1): 25-25.
- 469        Immerzeel, W. W., L. P. H. van Beek and M. F. P. Bierkens. 2010. Climate Change Will Affect the Asian  
470                Water Towers. *Science* 328(5984): 1382 LP-1385.
- 471        Li, X., G. Cheng, S. Liu, Q. Xiao, M. Ma, R. Jin, T. Che, Q. Liu, W. Wang, Y. Qi, J. Wen, H. Li, G. Zhu,  
472                J. Guo, Y. Ran, S. Wang, Z. Zhu, J. Zhou, X. Hu and Z. Xu. 2013. Heihe Watershed Allied Telemetry  
473                Experimental Research (HiWATER): Scientific Objectives and Experimental Design. *Bulletin of the*  
474                *American Meteorological Society* 94(8): 1145-1160.
- 475        Li, X., L. Wang, D. Chen, K. Yang and A. Wang. 2014. Seasonal evapotranspiration changes (1983–  
476                2006) of four large basins on the Tibetan Plateau. *Journal of Geophysical Research: Atmospheres*  
477                119(23): 13,13-79,95.
- 478        Liu, X., H. Zheng, M. Zhang and C. Liu. 2011. Identification of dominant climate factor for pan



- 479 evaporation trend in the Tibetan Plateau. *Journal of Geographical Sciences* 21(4): 594-608.
- 480 Ma, N., J. Szilagyi, Y. Zhang and W. Liu. 2019. Complementary-Relationship-Based Modeling of  
481 Terrestrial Evapotranspiration Across China During 1982–2012: Validations and Spatiotemporal  
482 Analyses. *Journal of Geophysical Research: Atmospheres* 124(8): 4326-4351.
- 483 Ma, W., Y. Ma and H. Ishikawa. 2014. Evaluation of the SEBS for upscaling the evapotranspiration based  
484 on in-situ observations over the Tibetan Plateau. *Atmospheric Research* 138: 91-97.
- 485 Ma, Y., Z. Hu, Z. Xie, W. Ma, B. Wang, X. Chen, M. Li, L. Zhong, F. Sun, L. Gu, C. Han, L. Zhang, X.  
486 Liu, Z. Ding, G. Sun, S. Wang, Y. Wang and Z. Wang. 2020. A long-term (2005–2016) dataset of  
487 hourly integrated land–atmosphere interaction observations on the Tibetan Plateau. *Earth Syst. Sci.*  
488 *Data* 12(4): 2937-2957.
- 489 Ma, Y., Z. Su, T. Koike, T. Yao, H. Ishikawa, K. i. Ueno and M. Menenti. 2003. On measuring and remote  
490 sensing surface energy partitioning over the Tibetan Plateau—from GAME/Tibet to CAMP/Tibet.  
491 *Physics and Chemistry of the Earth, Parts A/B/C* 28(1): 63-74.
- 492 Mauder, M. and T. Foken. 2015. Eddy-Covariance Software TK3.
- 493 Moore, C. J. 1986. Frequency response corrections for eddy correlation systems. *Boundary-Layer*  
494 *Meteorology* 37(1): 17-35.
- 495 Oki, T. and S. Kanae. 2006. Global Hydrological Cycles and World Water Resources. *Science* 313(5790):  
496 1068 LP-1072.
- 497 Pinker, R. T. and I. Laszlo. 1992. Modeling Surface Solar Irradiance for Satellite Applications on a  
498 Global Scale. *Journal of Applied Meteorology* 31(2): 194-211.
- 499 Shi, H., T. Li and G. Wang. 2017. Temporal and spatial variations of potential evaporation and the driving  
500 mechanism over Tibet during 1961–2001. *Hydrological Sciences Journal* 62(9): 1469-1482.
- 501 Stull, R. B. (1988). An introduction to boundary layer meteorology. Dordrecht, Kluwer Academic  
502 Publishers.
- 503 Su, Z. 2002. The Surface Energy Balance System (SEBS) for estimation of turbulent heat fluxes. *Hydrol.*  
504 *Earth Syst. Sci.* 6(1): 85-100.
- 505 Szilagyi, J., R. Crago and R. Qualls. 2017. A calibration-free formulation of the complementary  
506 relationship of evaporation for continental-scale hydrology. *Journal of Geophysical Research:*  
507 *Atmospheres* 122(1): 264-278.
- 508 Wang, B., Y. Ma, Z. Su, Y. Wang and W. Ma. 2020. Quantifying the evaporation amounts of 75 high-  
509 elevation large dimictic lakes on the Tibetan Plateau. *Science Advances* 6(26): eaay8558.
- 510 Wang, G., S. Lin, Z. Hu, Y. Lu, X. Sun and K. Huang. 2020. Improving Actual Evapotranspiration  
511 Estimation Integrating Energy Consumption for Ice Phase Change Across the Tibetan Plateau.  
512 *Journal of Geophysical Research: Atmospheres* 125(3): e2019JD031799-e032019JD031799.
- 513 Webb, E. K., G. I. Pearman and R. Leuning. 1980. Correction of flux measurements for density effects  
514 due to heat and water vapour transfer. *Quarterly Journal of the Royal Meteorological Society*  
515 106(447): 85-100.
- 516 Xu, C. Y. and V. P. Singh. 2005. Evaluation of three complementary relationship evapotranspiration  
517 models by water balance approach to estimate actual regional evapotranspiration in different climatic  
518 regions. *Journal of Hydrology* 308(1): 105-121.
- 519 Yang, K., H. Wu, J. Qin, C. Lin, W. Tang and Y. Chen. 2014. Recent climate changes over the Tibetan  
520 Plateau and their impacts on energy and water cycle: A review. *Global and Planetary Change* 112:



- 521 79-91.
- 522 Yang, W., X. Guo, T. Yao, K. Yang, L. Zhao, S. Li and M. Zhu. 2011. Summertime surface energy budget  
523 and ablation modeling in the ablation zone of a maritime Tibetan glacier. *Journal of Geophysical*  
524 *Research: Atmospheres* 116(D14).
- 525 Yao, T., H. Lu, W. Feng and Q. Yu. 2019. Evaporation abrupt changes in the Qinghai-Tibet Plateau during  
526 the last half-century. *Scientific Reports* 9(1): 20181-20181.
- 527 Yao, T., L. Thompson, W. Yang, W. Yu, Y. Gao, X. Guo, X. Yang, K. Duan, H. Zhao, B. Xu, J. Pu, A. Lu,  
528 Y. Xiang, D. B. Kattel and D. Joswiak. 2012. Different glacier status with atmospheric circulations  
529 in Tibetan Plateau and surroundings. *Nature Climate Change* 2(9): 663-667.
- 530 Zhang, C., F. Liu and Y. Shen. 2018. Attribution analysis of changing pan evaporation in the Qinghai-  
531 Tibetan Plateau, China. *International Journal of Climatology* 38(S1): e1032-e1043.
- 532 Zhang, K., J. S. Kimball, R. R. Nemani and S. W. Running. 2010. A continuous satellite-derived global  
533 record of land surface evapotranspiration from 1983 to 2006. *Water Resources Research* 46(9).
- 534 Zhang, T., M. Gebremichael, X. Meng, J. Wen, M. Iqbal, D. Jia, Y. Yu and Z. Li. 2018. Climate-related  
535 trends of actual evapotranspiration over the Tibetan Plateau (1961–2010). *International Journal of*  
536 *Climatology* 38(S1): e48-e56.
- 537 Zhang, Y., C. Liu, Y. Tang and Y. Yang. 2007. Trends in pan evaporation and reference and actual  
538 evapotranspiration across the Tibetan Plateau. *Journal of Geophysical Research: Atmospheres*  
539 112(D12).
- 540 Zhong, L., Y. Ma, Z. Hu, Y. Fu, Y. Hu, X. Wang, M. Cheng and N. Ge. 2019. Estimation of hourly land  
541 surface heat fluxes over the Tibetan Plateau by the combined use of geostationary and polar-orbiting  
542 satellites. *Atmos. Chem. Phys.* 19(8): 5529-5541.
- 543 Zou, M., L. Zhong, Y. Ma, Y. Hu, Z. Huang, K. Xu and L. Feng. 2018. Comparison of Two Satellite-  
544 Based Evapotranspiration Models of the Nagqu River Basin of the Tibetan Plateau. *Journal of*  
545 *Geophysical Research: Atmospheres* 123(8): 3961-3975.
- 546
- 547



548 **List of tables**

549 Table 1: Input datasets used in this study. .... 22

550 Table 2: Station information. .... 23

551

552



553

554 Table 1: Input datasets used in this study.

<b>Variables</b>	<b>Data source</b>	<b>Availability</b>	<b>Temporal resolution</b>	<b>Spatial resolution</b>
Downward Shortwave	CMFD	1979 – 2018	3 hours	0.1°
Downward longwave	CMFD	1979 – 2018	3 hours	0.1°
Air temperature	CMFD	1979 – 2018	3 hours	0.1°
Specific humidity	CMFD	1979 – 2018	3 hours	0.1°
Wind velocity	CMFD	1979 – 2018	3 hours	0.1°
Land surface temperature	MOD11C3	2001 – now	Monthly	0.05°
Land surface emissivity	MOD11C3	2001 – now	Monthly	0.05°
Height of canopy	GLAS & SPOT	2000 - now	Monthly	0.01°
Albedo	MOD09CMG	2001 - now	Daily	0.05°
<i>NDVI</i>	MOD13C2	2001 - now	Monthly	0.05°
DEM	ASTER GDEM	-	-	30 m

555

556



557

558 Table 2: Station information.

Station	Location	Elevation (m)	Land cover
QOMS	28.21°N, 86.56°E	4276	Gravel
NAMORS	30.46°N, 90.59°E	4730	Grassy marshland
SETORS	29.77°N, 94.73°E	3326	Grass land
NADORS	33.39°N, 79.70°E	4264	Sparse grass-Gobi
MAWORS	38.41°N, 75.05°E	3668	Sparse grass-Gobi
BJ	31.37°N, 91.90°E	4509	Sparseness meadow

559

560

561



562           **List of figures**

563   Figure 1: Locations of the six flux tower sites (marked by pentagrams) on the  
564   TP. The legend of the color map is elevation above mean sea level in meters.  
565   ..... 25

566   Figure 2: SEBS-estimated and EC - observed monthly  $ET_a$  at the six stations  
567   (a-f) on the TP in years when the latter observations were available. RMSE is  
568   the root-mean-square error, MB is the mean bias, and R is the correlation  
569   coefficient. .... 26

570   Figure 3: Spatial distribution of the SEBS-estimated multiyear (2001-2018)  
571   average annual  $ET_a$ . .... 27

572   Figure 4: Spatial distributions of the SEBS-estimated multiyear (2001-2018)  
573   average seasonal  $ET_a$  (mm/season) values over the TP. (a) spring, (b) summer,  
574   (c) autumn, (d) winter. .... 28

575   Figure 5: Spatial distribution of annual  $ET_a$  linear trend on the TP from 2001 to  
576   2018. The stippling indicates the trends that pass the t-test ( $p < 0.05$ ). .... 29

577   Figure 6: Spatial distributions of seasonal  $ET_a$  linear trends on the TP from 2001  
578   to 2018: (a) annual, (b) spring, (c) summer, (d) autumn, (e) winter. The stippling  
579   indicates the trends that pass the t-test ( $p < 0.05$ ). .... 30

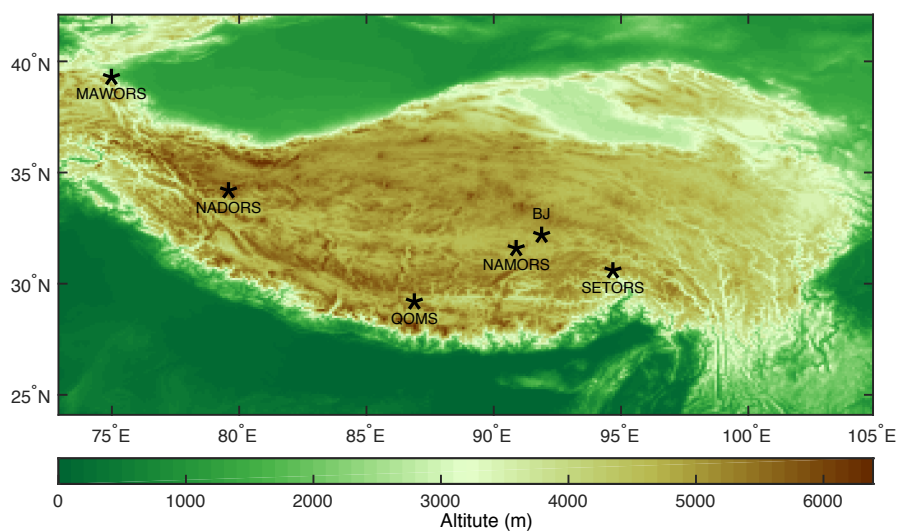
580   Figure 7: Anomalies of the domain-averaged annual  $ET_a$  of the entire TP, the  
581   western TP ( $\text{lon} < 90^\circ \text{ E}$ ), and the eastern TP ( $\text{lon} > 90^\circ \text{ E}$ ), respectively (a).  
582   Domain-averaged seasonal  $ET_a$  anomalies over the entire TP (b). The dashed  
583   straight lines indicate linear trends during 2001-2018, and  $k$  is the slope of the  
584   straight line. .... 31

585   Figure 8: Domain-averaged anomalies of annual  $R_n$  (a), precipitation (b), and  
586   temperature (c) over the entire TP, the western TP ( $\text{lon} < 90^\circ \text{ E}$ ), and the eastern  
587   TP ( $\text{lon} > 90^\circ \text{ E}$ ), respectively. The dashed straight lines indicate linear trends  
588   during 2001-2018, and  $k$  is the slope of the straight line. .... 32

589



590

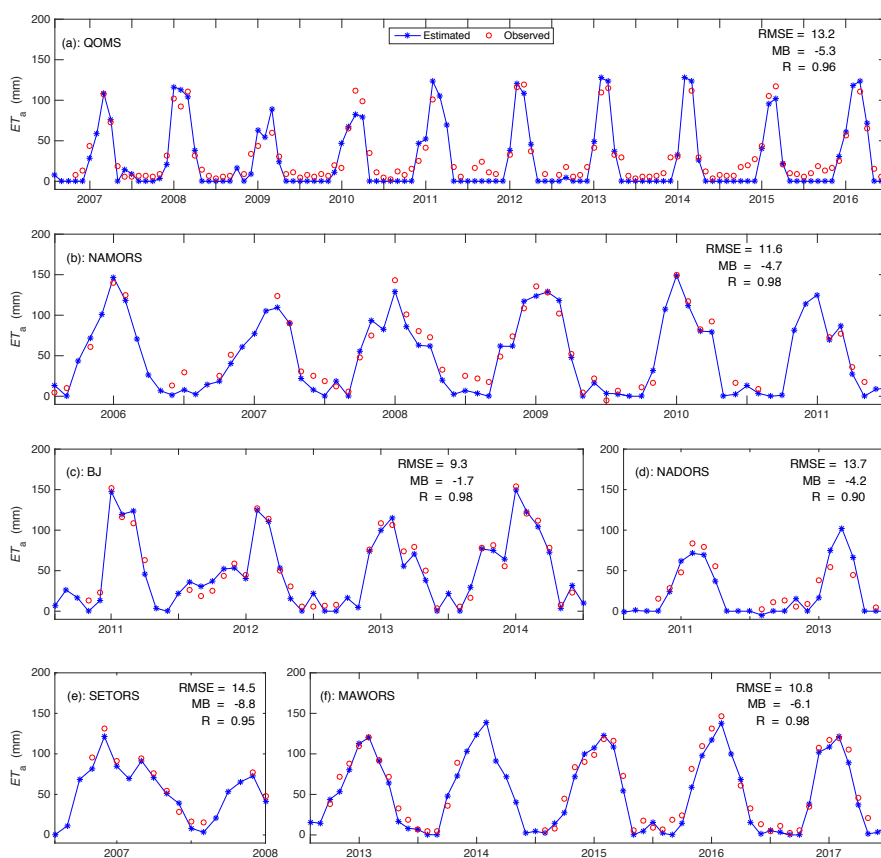


591

592 Figure 1: Locations of the six flux tower sites (marked by pentagrams) on the  
593 TP. The legend of the color map is elevation above mean sea level in meters.  
594



595



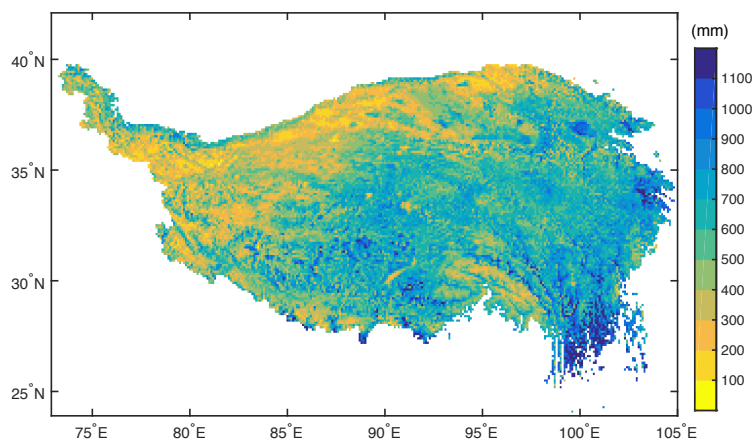
596

597 Figure 2: SEBS-estimated and EC-observed monthly  $ET_a$  at the six stations  
598 (a-f) on the TP in years when the latter observations were available. RMSE is  
599 the root-mean-square error, MB is the mean bias, and R is the correlation  
600 coefficient.

601



602



603

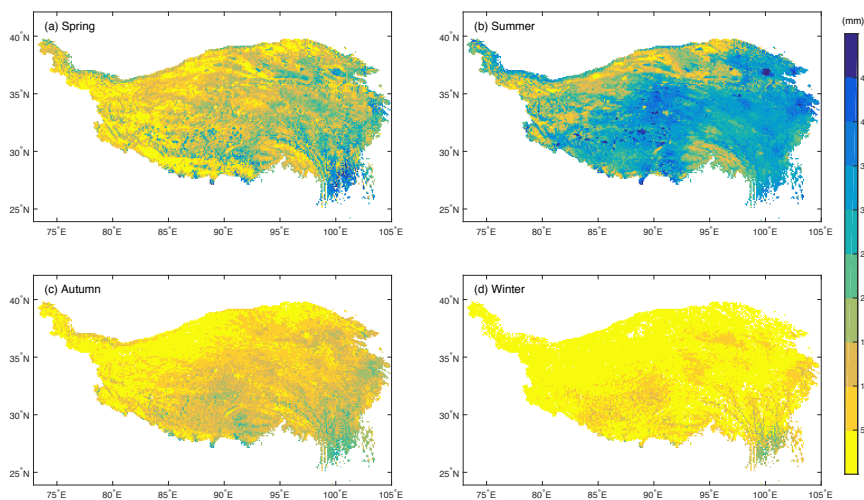
604 Figure 3: Spatial distribution of the SEBS-estimated multiyear (2001-2018)

605 average annual  $ET_a$ .

606



607



608

609 Figure 4: Spatial distributions of the SEBS-estimated multiyear (2001-2018)

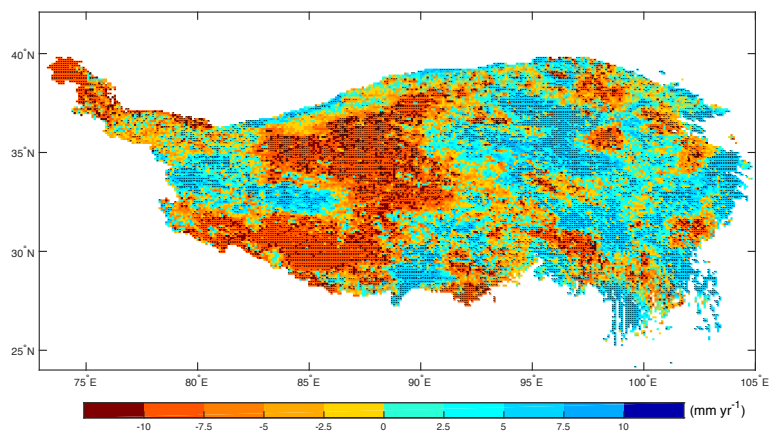
610 average seasonal  $ET_a$  (mm/season) values over the TP. (a) spring, (b)

611 summer, (c) autumn, (d) winter.

612



613



614

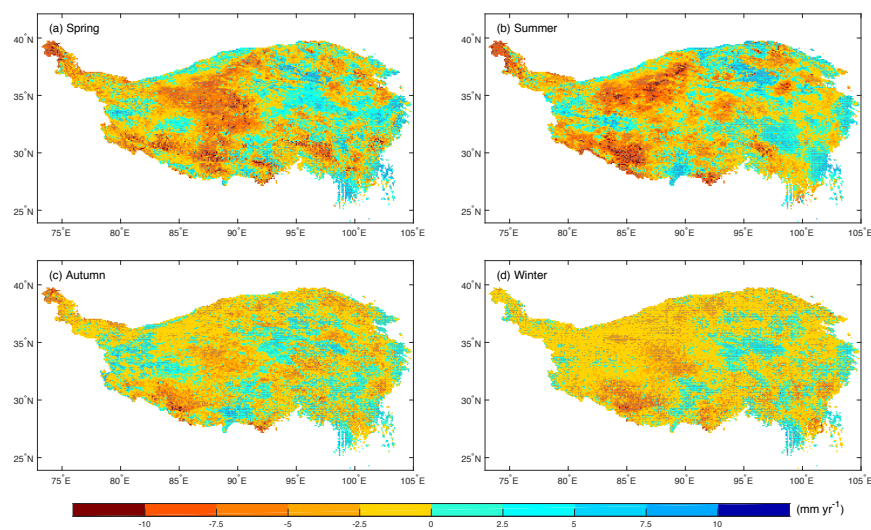
615 Figure 5: Spatial distribution of annual  $ET_a$  linear trend on the TP from 2001 to

616 2018. The stippling indicates the trends that pass the t-test ( $p < 0.05$ ).

617



618

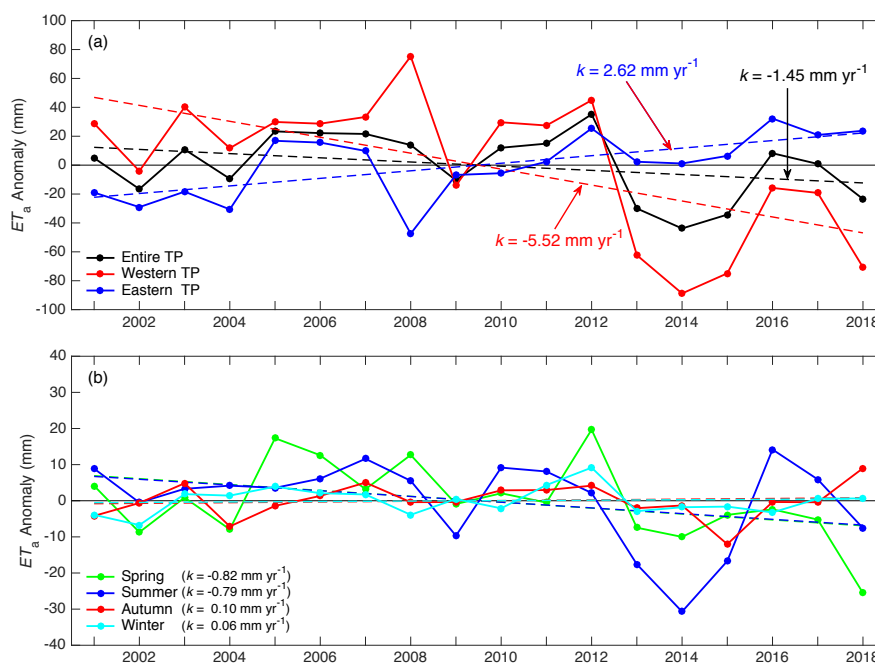


619

620 Figure 6: Spatial distributions of seasonal  $ET_a$  linear trends on the TP from  
621 2001 to 2018: (a) annual, (b) spring, (c) summer, (d) autumn, (e) winter. The  
622 stippling indicates the trends that pass the  $t$ -test ( $p < 0.05$ ).  
623



624



625

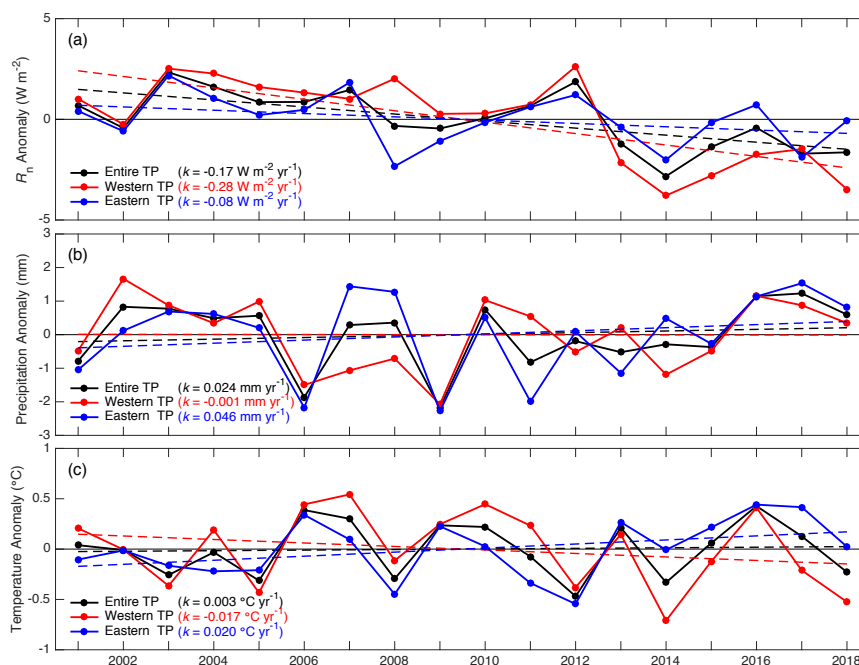
626 Figure 7: Anomalies of the domain-averaged annual  $ET_a$  of the entire TP, the  
627 western TP (lon < 90° E), and the eastern TP (lon > 90° E), respectively (a).  
628 Domain-averaged seasonal  $ET_a$  anomalies over the entire TP (b). The dashed  
629 straight lines indicate linear trends during 2001-2018, and  $k$  is the slope of the  
630 straight line.

631

632



633



634

635 Figure 8: Domain-averaged anomalies of annual  $R_n$  (a), precipitation (b), and  
636 temperature (c) over the entire TP, the western TP ( $\text{lon} < 90^\circ \text{E}$ ), and the  
637 eastern TP ( $\text{lon} > 90^\circ \text{E}$ ), respectively. The dashed straight lines indicate  
638 linear trends during 2001-2018, and  $k$  is the slope of the straight line.

639